nature electronics

Article

https://doi.org/10.1038/s41928-025-01482-3

A self-controlled reconfigurable intelligent surface inspired by optical holography

Received: 4 April 2024

Accepted: 17 September 2025

Published online: 29 October 2025



Jieao Zhu $lacktriangle ^{1,3}$ oxtimes, Ze Gu $lacktriangle ^{2,3}$ oxtimes, Qian Ma $lacktriangle ^{2}$ oxtimes, Linglong Dai $lacktriangle ^{1}$ oxtimes & Tie Jun Cui $lacktriangle ^{2}$ oxtimes

Reconfigurable intelligent surfaces operating at microwave frequencies are of potential use in the development of the sixth generation of wireless communications technology. Such surfaces could, in particular, be used to reprogram the wireless propagation channels in controlled ways and thus provide low-cost wireless capacity boosting, coverage extension and enhanced energy efficiency. To reprogram the channel, each meta-atom of the reconfigurable intelligent surface needs to receive an external control signal, which is usually generated by a base station. However, this requires complicated control cables, which restricts wide deployment. Here we report a self-controlled reconfigurable intelligent surface that is inspired by optical holography. Each meta-atom of the reconfigurable intelligent surface is integrated with a power detector that can record a hologram created from simultaneous microwave illumination from the base station and the user. We use classical Fourier transform to process the measured hologram and retrieve the angular position of the user, which is required for beamforming. As a result, the approach can provide autonomous reconfigurable intelligent surface beamforming without control cables.

The sixth generation of wireless communication systems should have high data rates and wide wireless coverage to support applications such as augmented reality¹, digital twins² and autonomous driving³. The development of such technology typically focuses on transceiver designs, but artificially reconfiguring the wireless channel to provide favourable propagation conditions is another promising approach^{4–10}. Due to progress in metamaterials and metasurfaces ^{5,6,9,11–14}, reconfigurable intelligent surfaces (RISs) have, in particular, been proposed to directly manipulate the channel for enhanced wireless transmissions.

An RIS is a planar array typically composed of multiple low-cost nearly passive tunable meta-atoms, which can tune the amplitude, phase, frequency, polarization and other electromagnetic (EM) characteristics of incident signals^{7,12}. By configuring these meta-atoms, RISs can alter the wireless channel between the base station (BS) and the user equipment (UE), thereby overcoming shadowing and deep fading problems commonly encountered in complicated propagation environments such as dense urban areas¹⁰. RIS could, therefore, extend

the coverage¹⁵, save hardware cost¹⁶ and reduce power dissipation¹⁷ of future sixth-generation wireless systems.

RIS control mechanisms include thermal¹², optical¹⁸, gyroscopic¹⁹ and visual^{6,20} mechanisms. In real-world wireless systems, these physical control mechanisms need to adapt to the fast-varying propagation environment¹⁰. Therefore, a system-level RIS control method needs to support real-time adaptation. Such adaptation usually requires control signals generated by a BS, which are then transmitted through wireless or wired control links to the RISs. For wireless control, complicated radio-frequency (RF) receivers and extra baseband processors are required at each RIS^{21,22}, and as the system scales, this has a negative impact on the low-cost benefit of RISs. Thus, wired control is a more common practice. However, wired control still requires at least one additional control cable per deployed RIS, which limits remote installation and wide deployment. Self-adaptive metasurfaces with dual sensing and beamforming capabilities do not need such BS–RIS control links²³. However, this self-adaptive method requires prior collected

¹Department of Electronic Engineering, Tsinghua University, Beijing, China. ²State Key Laboratory of Millimeter Waves, Southeast University, Nanjing, China. ³These authors contributed equally: Jieao Zhu, Ze Gu. —e-mail: zja21@mails.tsinghua.edu.cn; guze@seu.edu.cn; maqian@seu.edu.cn; daill@tsinghua.edu.cn; tjcui@seu.edu.cn

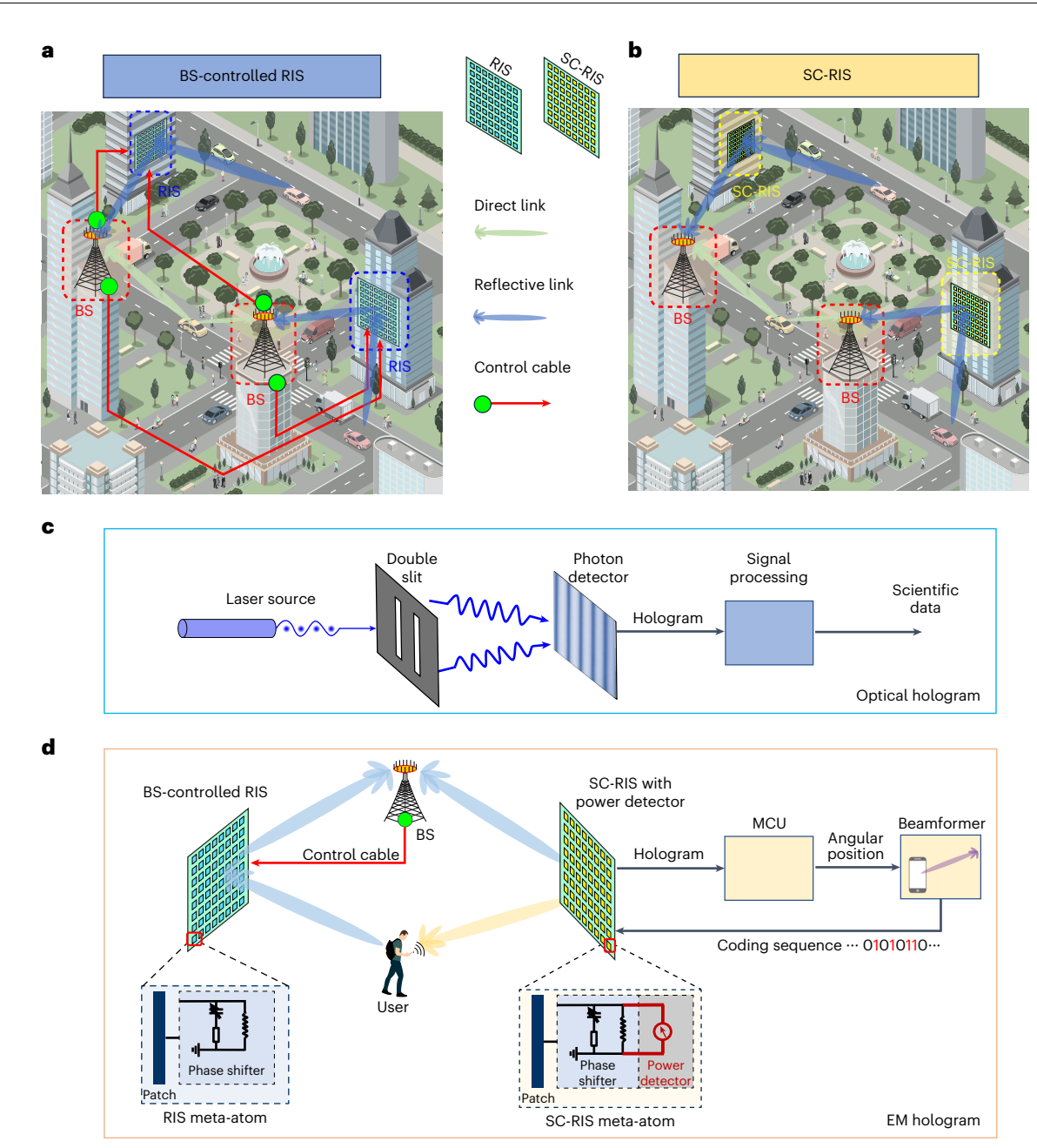


Fig. 1 | **Overall schematic of holography-inspired SC-RIS. a**, RISs are usually deployed on urban building facets to dynamically overcome shadowing by providing additional reflective links. Traditional RISs are wire-controlled by the BS, thereby incurring a complicated control cable cost. **b**, Our SC-RIS is capable of 'cutting' the control cable and acting as a self-controlled smart reflective

beamformer. \mathbf{c} , Workflow of the optical holography experiment. \mathbf{d} , Inspired by optical holography, the SC-RIS can measure the incident EM intensity (hologram) via an additional power detector array, and self-configure its phase shift for beamforming according to the processed hologram. Credit: background illustration in \mathbf{a} @ Mizhi.com.

channel data that depends on the specific propagation environment, which complicates system-level deployment.

In this Article, we report a self-controlled RIS (SC-RIS) for wireless localization based on holographic principles²⁴. To compensate for the absence of a control line, the control signal needs to be self-generated by the RIS, which requires the RIS to self-determine the user's angular location, including the azimuth and elevation angles. Each meta-atom in our SC-RIS is additionally equipped with a power detector²⁵. The power detectors record a hologram that contains the entire EM wavefront information. On the basis of the holographic recording principle²⁶, the user angle can be determined without an RF receiver. The user's angular location can be computed by applying a two-dimensional (2D) fast Fourier transform (FFT) to the measured

hologram. With this user's angle information, beamforming algorithms executed by the RIS can steer the beams towards the user's direction. We show that the accuracy of the angular location estimation approaches the theoretical array resolution limit and that our SC-RIS enhances the average received power by 16.4 dB in a practical wireless communication system. Since no control signals and precollected data are needed during angular estimation and RIS beamforming, the SC-RIS can cooperate with other communication devices in a fully autonomous manner.

Working principle

Figure 1 shows a schematic of our holographic-principle-based SC-RIS system, which is independent of the control by BS (Fig. 1a,b). The SC-RIS is capable of automatically enhancing the communication links without

a control cable. To achieve this self-controllability, it is necessary to sense the EM environment in an efficient and low-cost way. Inspired by the optical holographic interference experiment shown in Fig. 1c, we create an EM hologram at the SC-RIS by simultaneous microwave illuminations from both BS and user. As shown in Fig. 1d, our SC-RIS consists of an array of dual-functional meta-atoms. Like the traditional RIS, each meta-atom works as a space-fed tunable reflective phase shifter. Additionally, the meta-atoms of SC-RIS are equipped with power detectors to record the EM hologram. Since the hologram contains the user's location information, a holographic localization algorithm is then executed to estimate the user angular location. Finally, with the estimated user location, a coding sequence is generated to control the phase shifts of each meta-atom to fulfil collaborative beamforming to an arbitrary user, achieving the SC-RIS's closed-loop self-controllability.

To achieve a holographic measurement, the entire EM intensity information on the whole SC-RIS is required. Thus, the holographic sensing apparatus needs to be both widely spread across the surface and closely integrated into each meta-atom. To satisfy these two technical needs, we adopt the hardware-structure multiplexing method in the meta-unit design that successfully solves the problems by integrating the sensing circuit into the meta-unit^{25,27} (Fig. 2). Through this integration, the meta-unit constituting the SC-RIS is entitled with sub-wavelength sensing capability, which senses the EM field on the same scale as its EM manipulation capability. In Fig. 2a, we show a simplified diagram of the designed meta-unit with principal illumination. Most of the energy that impinges on the meta-unit is reflected with a 1-bit phase modulation empowered by the active resonant structure controlled by two PIN diodes, whereas a small fraction of energy (-10 dB) is coupled into the power detectors. Diode-control and voltage-readout circuits are embedded inside each unit, whose routings are carefully designed to avoid coupling between these two parts of different functionalities (Fig. 2b). In the unit design, we optimize the geometry of the metallic patches as well as the impedance matching of the power detectors to minimize the adverse effect on reflection efficiency. Full-wave simulation result demonstrates that the introduced amplitude loss (S_{11}) is less than 0.5 dB compared with RIS units without sensing structures.

Figure 2c,d depicts the frequency response of the unit's reflective parameter and detector voltage output. Around the central frequency, a 220-MHz bandwidth is realized for a 180° phase difference between the two states within a 20° range. The sensitivity of the meta-unit reaches its maximum at the frequency of approximately 3.1 GHz (Fig. 2d, inset), which depicts the voltage-frequency relationship under a certain injection power level. The minor deviations between the valid frequency bands may arise from detuning inside the matching network. Nevertheless, the discrepancy only leads to a small drop in the detector output voltages, which are still able to be collected by analogue-to-digital converters (ADCs). Meanwhile, from the curves shown in Fig. 2d, it is evident that the power sensing performance is also limited by the dynamic range of the detectors, whereas a low-power energy injection could not be identified. In real application scenarios, microwave amplifiers or automatic gain control modules will be added, which can amplify the coupled energy and retain the relative intensity magnitudes among different sensing nodes.

To achieve self-controlled autonomy, the location information of the user is required at SC-RIS. Thus, we design the holographic localization algorithm, which is responsible for extracting the location information of each user from the measured hologram. To create the hologram containing the user location, we allow two coherent EM sources (BS and UE) to simultaneously illuminate the SC-RIS (Fig. 3a). Note that this method strictly follows the holographic imaging principle 26 . On one hand, the EM signal from BS plays the role of reference wave, which is denoted as β . Since BS is usually installed at a known location in the communication environment, β is assumed to be known to the microcontroller unit (MCU). On the other hand, the EM signal

from the user corresponds to the object wave in holographic imaging, which is denoted as α . The hologram intensity I is, thus, created by the EM interference between α and β waves, which is represented as

$$I_{mn} = \left| \alpha_{mn} + \beta_{mn} \right|^2, \tag{1}$$

where indices m and n indicate the row and column of the hologram, respectively.

To extract the user angles from the hologram, it is necessary to study its structural characteristics. Assuming that the BS and UE are in the far-field region of the SC-RIS, we analyse the spectral properties of the hologram in the spatial frequency domain (k domain), which can be efficiently computed by FFT. Figure 3b illustrates the three-peak spectral characteristics of a simplified one-dimensional (1D) hologram. In this spectral representation, the BS signal $\boldsymbol{\beta}$ (red) interferes with the UE signal $\boldsymbol{\alpha}$ (blue), creating a hologram with three peaks in k space (pink). Two symmetric peaks originate from the differential frequencies between the BS and UE signals, and the zero-frequency peak is determined by the total signal energy of the hologram (Supplementary Note 1 provides the proof of the three-peak spectral structure). Since the symmetric peaks are determined by the unknown UE location and the known BS location, the detection of symmetric peaks will help retrieve the UE location.

By exploiting the three-peak spectral structure of the EM hologram, we design a holographic localization algorithm (Fig. 3c). The algorithm relies on a 2D-FFT analysis on the hologram. Specifically, by expanding equation (1), the two squared terms $|\alpha_{mn}|^2 + |\beta_{mn}|^2$ correspond to the zero-frequency part of the holographic spectrum, whereas the cross-terms $\alpha_{mn}^*\beta_{mn} + \alpha_{mn}\beta_{mn}^*$ encode the interference between the target UE and the reference BS, contributing to the two differential frequency peaks. By applying a spatial FFT, these interfering terms are converted into the differential frequencies in k space, which is expressed as

$$\hat{I}_{k\ell} = \text{FFT}[I_{mn}]_{k\ell} = A\Delta_{k\ell}(0,0) + (C\Delta_{k\ell}(\Delta_z, \Delta_x) + C^*\Delta_{k\ell}(-\Delta_z, -\Delta_x)),$$
(2)

where Δ_z and Δ_r are the spatial frequency differences of α and β in the z and x directions, respectively. The zero-frequency term in equation (2) represents the average intensity A of the hologram, and the second term represents the spatially varying structure of the hologram. Thus, by performing a 2D-FFT on the hologram I_{mn} , we can retrieve the spatial frequency differences Δ_z and Δ_x from the spectral peaks in $\hat{I}_{k\ell}$. Since the spatial frequencies are uniquely determined by the user's incident angles, we can finally compute the angular location $(\theta_{UF}, \varphi_{UF})$ of the unknown target from the observed hologram (the Methods provides the algorithm details). However, the spectral peaks in $\hat{I}_{k\ell}$ appear in pairs, indicating that there are two candidate solutions to the user localization problem. This is caused by the indistinguishability between the two interfering cross-terms $\alpha_{mn}^*\beta_{mn} + \alpha_{mn}\beta_{mn}^*$. This ambiguity is known as the twin image problem in optical holography²⁶. Fortunately, the twin image can be removed by the regulated compressed sensing-based algorithms²⁸ or by joint user localization from multiple phase-shifted holograms with phase-shifted reference waves²⁹ (Supplementary Note 2). As a result, unless applied to the extremely time-sensitive case in which multiple holographic measurements are unacceptable, the twin image problem will not substantially affect the holographic localization algorithm.

The simulated accuracy of the 2D-FFT algorithm is provided in Supplementary Note 3, which has been compared with high-complexity super-resolution algorithms such as maximum-likelihood estimators. Furthermore, the robustness of the algorithm against the BS-UE power unbalance is discussed in Supplementary Note 4. In addition, we note here that no strict synchronization is required for the carrier frequency from two terminals. The frequency deviation would cause a temporal

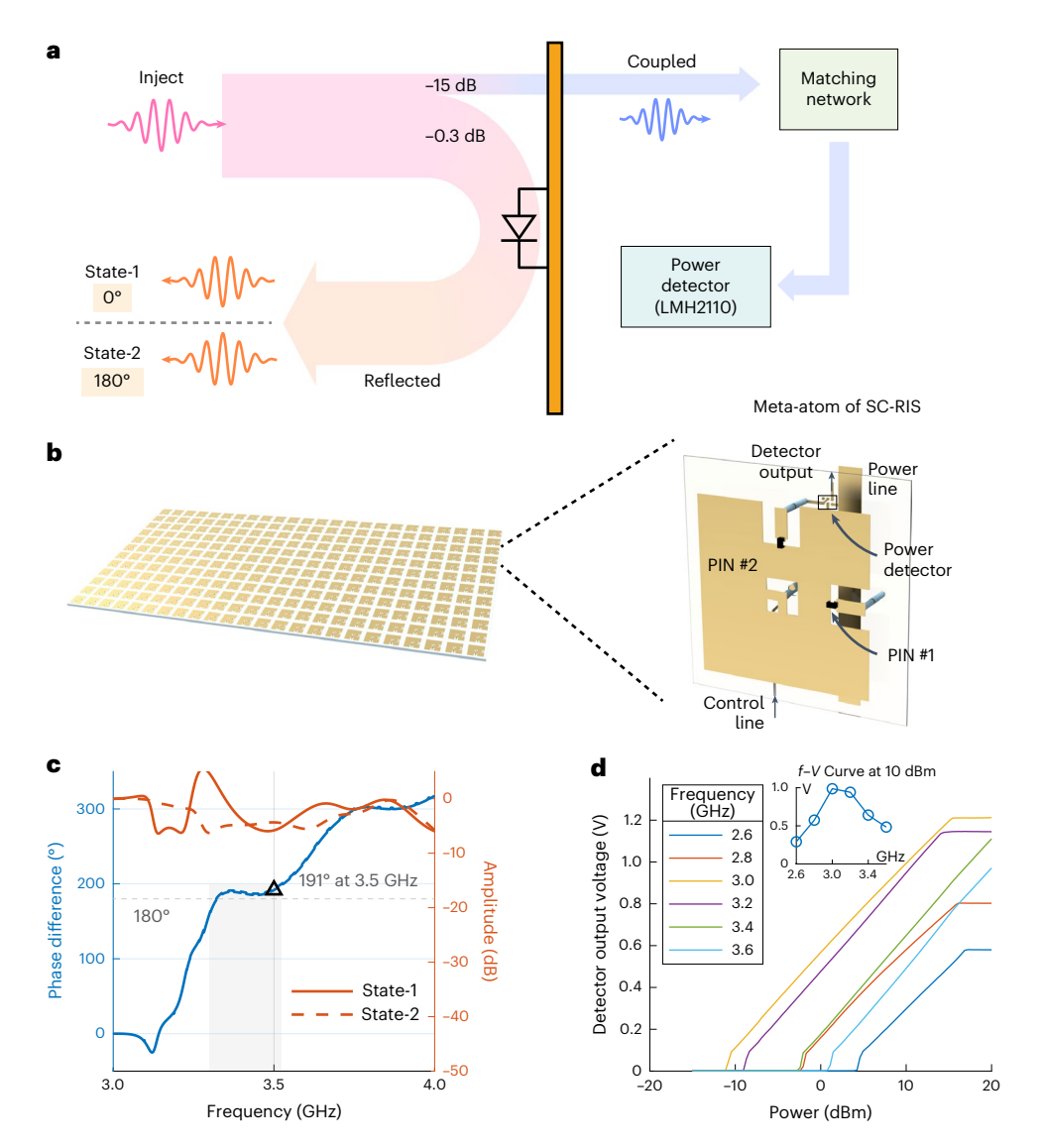


Fig. 2 | Meta-unit with dual EM sensing—manipulation functionality. a, Mechanism of the meta-unit. Similar to a traditional reflective meta-unit, most injected EM energy is reflected through the unit that has a 1-bit phase modulation ability, marked by State-1 (PIN in the conduction state) and State-2 (PIN in the cut-off state) in the figure. A fixed amount of injected energy is coupled into the integrated detector inside the unit, passing through a matching network mid-way for impedance matching, **b**, Demonstration of the 32×32

SC-RIS and the magnified picture of the unit model $(2 \text{ cm} \times 2 \text{ cm})$. **c**, Measured reflective parameters under two states. Around the centre frequency, a 220-MHz bandwidth is realized for a 180° phase difference between the two states under a 20° deviation. **d**, Measured detector output voltages of the meta-unit under EM wave illumination of different intensities and frequencies. The inset shows the frequency versus voltage (f-V) for a certain power level, validating the resonant position of the sensing circuit design.

periodical drift in the holographic patterns, which, in principle, would not affect the localization result (Supplementary Note 5).

User localization and wireless communication performance

Figure 4 shows the experimental setup of holographic localization and the corresponding results. First, a 32 × 32-unit SC-RIS is fabricated with an overall size of 0.64 × 0.64 m² and placed in the *xOz* plane for EM sensing and channel augment (Fig. 4a). Meanwhile, two terminals—UE and BS—are characterized by two antennas that target the SC-RIS as independent radiation sources. To be specific, the UE terminal represents the moving target that to be localized and the BS terminal represents the stationary reference point whose location is considered prior information to the algorithm. The communication link between the UE and BS is also established, where the UE terminal becomes a receiver that collects the signal generated by the BS. In the built-up system, an RF SP2T switch is connected to the UE antenna that guides

the energy direction from the signal generator (in the localization mode) or into the spectrum analyser (in the communication mode). Two modes alternate between each other temporally, constructing a continuous detecting–targeting loop for moving terminals.

A three-level hierarchy for our system is plotted in Fig. 4b for a plain demonstration. At the bottom layer, that is, the application layer, algorithms of our non-coherent localization as well the coding generation for SC-RIS are implemented on the processor unit. A set of peripherals inside the processor manages the data flow from or towards the peripheral modules, including an ADC array, a diode driver circuit and a graphical user interface display in the control layer (Methods). In the experiments, we first use single-tone signals as excitations for two terminals. Without loss of generality, the single-tone excitation represents the simplest and most-efficient way for interference generation and could be easily analysed by the spectrum analyser quantitatively in simulated communication for channel estimation. In the transmission layer, the antennas are positioned in a fashion that no

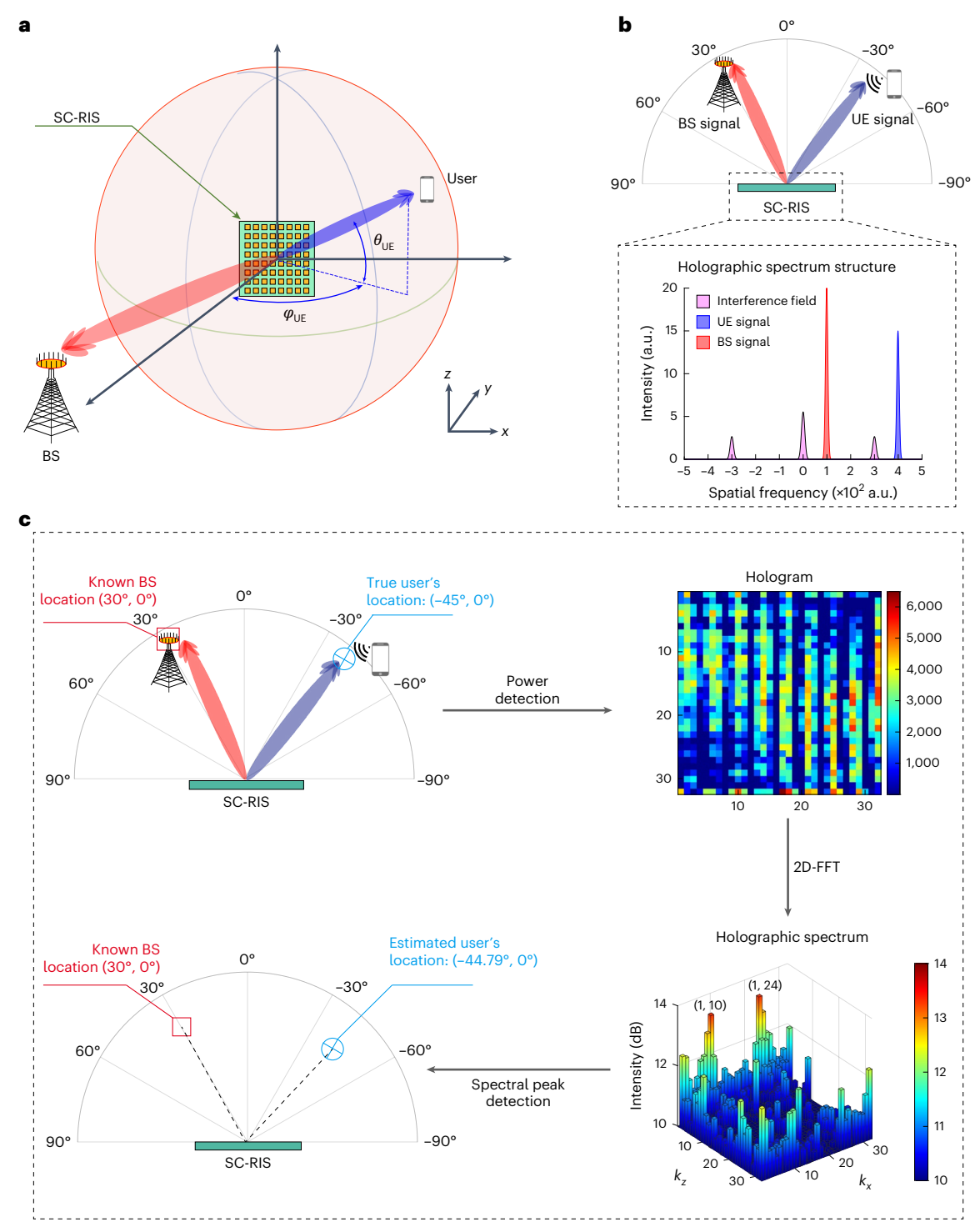


Fig. 3 | **Holographic localization algorithm. a**, Coordinate system for the analysis of SC-RIS. The SC-RIS is placed in the xOz plane at the origin, where the unknown location of the UE is described in spherical coordinates. **b**, Spectral characteristics of the hologram, viewed along the x axis. In the spatial frequency domain (k space), the hologram contains three spectral peaks: the two symmetric differential frequencies that arise from mutually interfering terms, and the

zero-frequency peak that comes from the self-interfering term. \mathbf{c} , Schematic of obtaining the user's angular location (φ,θ) by the holographic localization algorithm. The colour represents the digital value of the ADC readout. To exploit the three-peak structure of the holographic spectrum, 2D-FFT is applied to the hologram. The angular location of the user can be determined from the spectral peaks that correspond to the two differential frequencies.

direct-line-of-sight path exists in an analogue of obstacle scenarios. The SC-RIS acts as the spatial modulator for channel augment inside the communication link.

To facilitate the result presentation, the middle variables inside the algorithms are collected and demonstrated (Fig. 4) together with the final localization results. Three samples are chosen, where the BS and UE are located at three different locations. As a demonstration for non-coherent holographic detection, our holographic localization algorithm only relies on the intensity information inside the monitoring plane (Fig. 4c). We could clearly observe the interference patterns, that is, the hologram, that marks the periodical amplitude fluctuation along the y axis. On the basis of the principle of the holographic

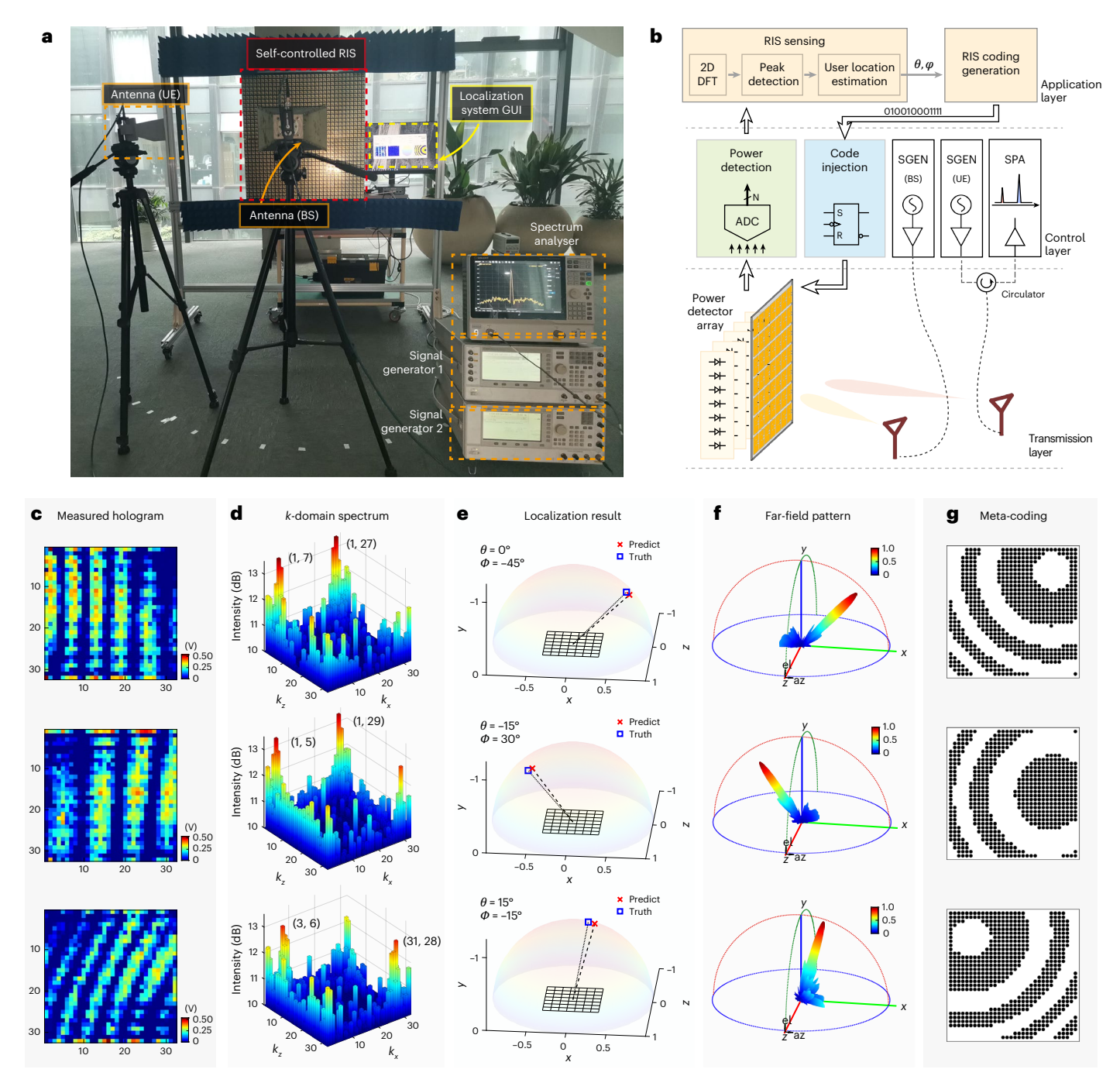


Fig. 4 | **Holographic localization experiment. a**, Photograph of the system. Two radiation terminals are characterized by two antennas, which represent a user that is to be localized (UE) and a fixed-position BS. Each terminal is connected to a signal generator independently. In the localization experiment, single-tone signals of the same frequency are excited from the antennas. The SC-RIS monitors the interference field dynamically via the integrated sensing nodes and updates its coding for channel enhancement according to the in situ localization result. GUI, graphical user interface. UE, user equipment; BS, base station. **b**, System diagram for simultaneous localization and channel augment.

SGEN, signal generator; SPA, spectrum analyzer; DFT, discrete Fourier transformation. **c**, Detector array outputs. Three samples are chosen for demonstration. As a demonstration for non-coherent detection, our localization algorithm only relies on the intensity information inside the monitoring plane, which substantially simplifies the system. **d**, *k*-domain spectra after 2D-FFT, where the amplitude peaks that represent the interference can be clearly identified. **e**, Predicted location of the user. The actual position is given for reference. **f**, Far-field patterns with focusing beams targeted at the UE position after channel augment. **g**, Optimized coding patterns.

reconstruction algorithm, the peaks of the Fourier transform hologram represent the relative angular position of the two radiation points (Fig. 4d). The peaks in the spectrum exist in pairs, which matches the two possible solutions caused by the twin image problem, which is previously explained in the algorithm description. Finally, the predicted locations of the UE terminal are derived and demonstrated in Fig. 4e. The actual positions are given for reference, where the

localization error is around 4° for the three samples. The bended strips are caused by the uneven amplitude illumination from the terminals located in the semi-near region. Despite the fact that the numeric model is built on far-field assumptions, the algorithm still retrieves the location correctly based on the experiment results. The result proves the robustness of our holographic localization method (Supplementary Note 6).

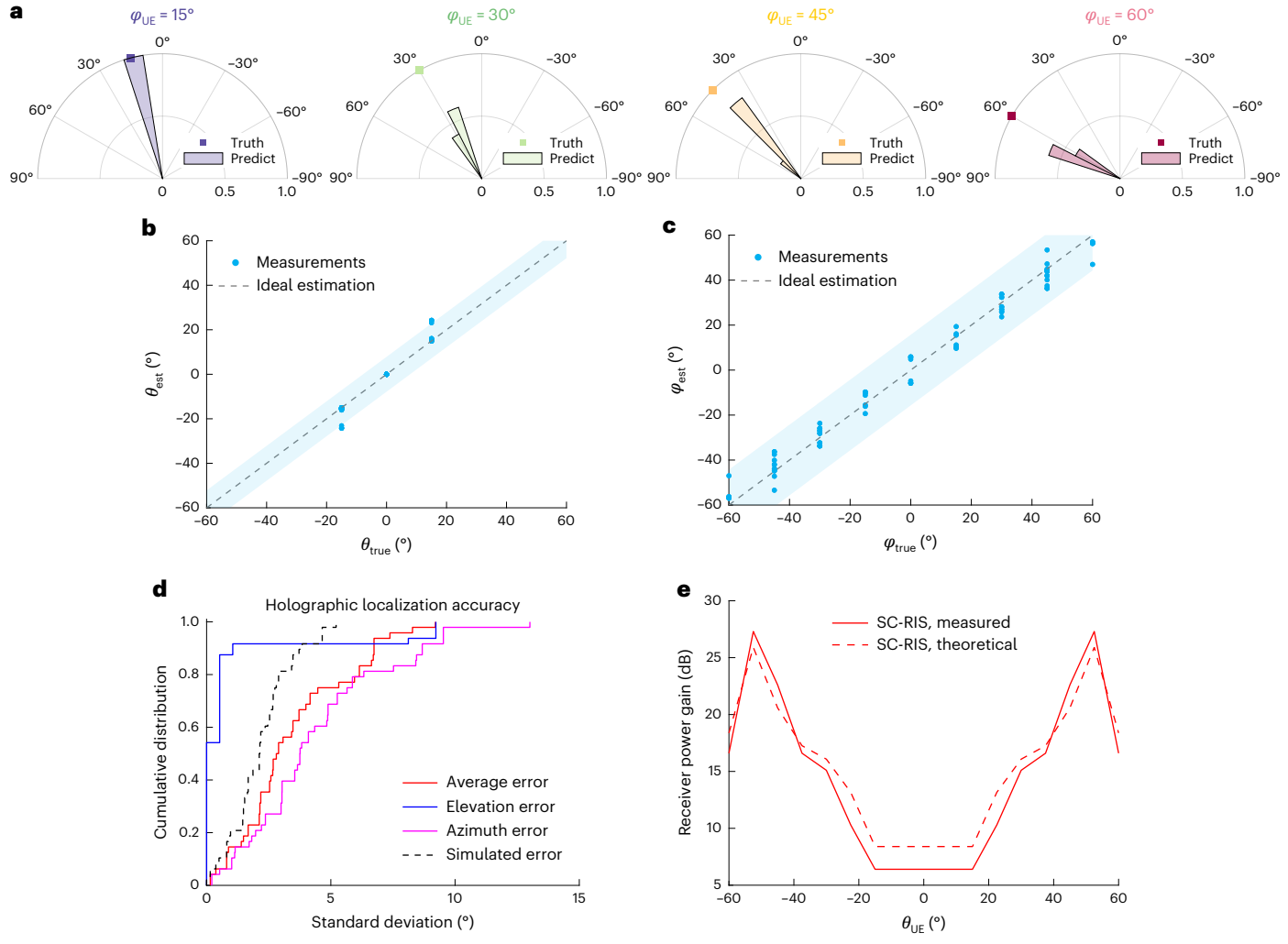


Fig. 5 | **System performance of SC-RIS. a**, Distribution of the SC-RIS localization results with users at different angular locations. **b**, **c**, Measured SC-RIS localization performance, compared with ideal estimators (dashed) that produce the estimated angles φ_{est} , θ_{est} that are identical with the true values φ_{true} , θ_{true} ,

respectively. The blue-shaded region represents the range of ± 3 standard deviation. ${\bf d}$, Measured localization performance compared with the simulation. ${\bf e}$, User's received power gain after activating the SC-RIS. An average improvement of 16.4 dB is observed when the SC-RIS is enabled.

The experimental results for channel augment are also provided in Fig. 4. The field converging capability is demonstrated through the focusing patterns shown in Fig. 4f, where the transmission parameter between the UE and BS terminals is improved by at most 20.1 dB. In Fig. 4g, the near-field codings are adopted for their better EM energy converging performance. Here we adopt the near-field coding mechanism to achieve an optimal channel enhancement performance. The expenses of this method include a higher calculation cost in coding generation and a demand for distance information. However, such defects could be overcome with an introduction of high-performance processors and parallel architecture for distance estimation algorithms, which have been studied extensively 30.

Following the procedures in Fig. 4b, the overall system can realize non-coherent detection and automatic encoding through a self-programming metasurface without any human intervention. Supplementary Video 1 presents a solid demonstration of such autonomous procedures. It should be noted that our SC-RIS system may reach the lower bound of RF detectors in a low-received-signal-strength environment. However, with the introduction of customized hardware improvements and signalling protocols, we demonstrate that our system could reach a maximum detection range of over 20 m under modern wireless communication standards (Supplementary Notes 7 and 8).

Before carrying out the real communication experiments, a comprehensive analysis is first presented concerning the system performance.

To quantify the user localization capability of our SC-RIS, we show the estimation accuracy of the user's angular location $\theta_{\text{UE}}, \varphi_{\text{UE}}$ by running our holographic localization algorithm on the MCU to process the measured data in real time. In the testing scenario, the BS antenna is placed at four different possible locations $(\theta, \varphi)_{\text{BS}}$ of $(0^\circ, 0^\circ), (-15^\circ, 0^\circ), (-15^\circ, -30^\circ)$ and $(0^\circ, -30^\circ)$; although the UE antenna is placed at locations $(\theta, \varphi)_{\text{UE}}$ of $\theta_{\text{UE}} \in \{0^\circ, \pm 15^\circ\}$, and $\varphi_{\text{UE}} \in \{0^\circ, \pm 15^\circ, \pm 30^\circ, \pm 45^\circ, \pm 60^\circ\}$, except for the locations that coincide with the BS. For each allowable BS–UE location configuration, the hologram is digitally measured by SC-RIS, and the holographic localization algorithm (Algorithm 1) is executed to obtain the estimated UE location $(\theta, \varphi)_{\text{esc}}$.

The localization performance is demonstrated in Fig. 5a when the user is fixed at $\varphi_{UE} \in \{15^\circ, 30^\circ, 45^\circ, 60^\circ\}$. Data are gathered by varying the location of the BS antenna and taking multiple observations for each BS–UE configuration. From Fig. 5a, we observe that the holographic localization algorithm returns angle estimates with an error of $\leq 9^\circ$ with high probability, coinciding with the simulated results in Algorithm 1. Figure 5b illustrates the estimated user's elevation angle $\theta_{\rm est}$ with respective to SC-RIS, compared with the ideal estimator (dashed line). Similarly, the estimation results for the azimuth angle φ

are shown in Fig. 5c. Since the manufactured SC-RIS is a square array with x and z symmetry, the estimated results shown in Fig. 5b,c are also symmetric relative to the central point $(0^{\circ}, 0^{\circ})$.

To statistically characterize the performance of holographic localization, we further compute the error distribution of the angular estimators. The standard deviation values are 2.61° for the elevation angle and 5.24° for the azimuth angle, compared with the theoretical resolution limit of 6.62° for a 32 × 32-element array on each dimension (Supplementary Note 9 provides the definitions of array resolution). Since the azimuth angle is estimated after the elevation angle in the 2D-FFT algorithm (Methods), the azimuth deviation is larger than the elevation deviation due to error accumulation. The total average angular deviation of the estimator is 5.85°, which effectively approaches the 6.62° array resolution limit. The small error of the 2D-FFT holographic localization algorithm is attributed to power detector noise and indoor multipath effect. The cumulative distributions of the measured estimation errors are shown in Fig. 5d, together with that of the simulated data obtained by performing 2D-FFT on the noiseless theoretical interference pattern (dashed). By comparing the red measured curve with the dashed simulated curve, we conclude that our user localization algorithm shows comparable performance against the ideal simulated case, even though the measurements are influenced by the detector noise and multipath effect (Supplementary Note 10).

To further verify the autonomous beamforming capability of our SC-RIS, we conduct fully automated experiments with the MCU-executed holographic detection and beamforming pipeline. The measured results shown in Fig. 5e exhibit an average improvement of 16.4 dB in the user-received power when the automatic encoding on SC-RIS is activated. The received power is consistently improved across the azimuth angles from -60° to 60° , showing a stable reflective gain of the incident continuous microwave without data modulation. The data trend of the measured gain effectively coincides with the theoretical predictions. Notice that the theoretical predictions are compensated by taking into consideration the insertion losses of the signal generators, antennas and circulators involved in the field-test experiments.

To demonstrate the communication-enhancing functionality of the SC-RIS, we test the autonomous beamforming function with an orthogonal frequency-division multiplexing (OFDM) transceiver implemented on two software-defined radio (SDR) platforms, simulating a real-world communication system. Here the SC-RIS is configured to the autonomous beamforming mode, indicating that it can enhance the BS-user communication link without the control cable. Figure 6a shows the wireless communication experimental settings, in which data transmission is aided by the fabricated SC-RIS. The SC-RIS is placed in front of the transmitter and receiver antennas to provide a controllable reflective link. We test the data transmission functionality with two 24-bit true-colour logos of Tsinghua University and Southeast University. The data are 1.74 Mbit in total and are transmitted with a fixed transmission power of -50 dBm, simulating a mobile communication scenario with a typical received power of -90 dBm. The key technical parameters are summarized in Fig. 6b.

To show the autonomous link enhancement capability of the SC-RIS, we transmit the same picture data with different configurations of SC-RIS. In Fig. 6c,d, we test the SC-RIS beamforming capability by scanning its beamforming angle from –60° to 60°, where the user is fixed at 30° and 45°, respectively. During the angle scanning of SC-RIS, the received baseband signals are continuously recorded and processed by the receiver SDR; the bit error rate (BER) of each SC-RIS beamformer configuration is presented in Fig. 6c. The BER exhibits a waterfall-like drop at the true UE angles, demonstrating the link enhancement capability of the SC-RIS under correct user angular estimation. The corresponding received RF power versus the SC-RIS beamforming angle is presented in Fig. 6d, compared with the

received power when the SC-RIS is OFF. An average received power boost of 12 dB is achieved by SC-RIS on correct angular estimation of the user.

To quantify the communication performance improvement brought by SC-RISs, we present detailed measurement results obtained from the full OFDM signal processing pipeline, where the intermediate results are shown in Fig. 6e-g. In Fig. 6e-g, the SC-RIS is tested in four different modes, including autonomous beam alignment, misalignment of 7°, misalignment of 31° and random configuration, from top to bottom. The user is fixed at an angle of 45°. Figure 6e shows the first 2,000 received data symbols (in coloured dots), compared with the ideal constellation positions (in red +). The received symbol noise decreases substantially when the SC-RIS performs autonomous beam alignment. Figure 6f shows the estimated channel frequency response (CFR) as a function of the subcarrier frequency. The CFR estimation accuracy improves when the SC-RIS beam is autonomously aligned to the user. Finally, the received data payload, that is, the image logos, are demodulated and shown in Fig. 6g together with the signal-to-noise ratio averaged over all the subcarriers. The quality of the received image improves substantially when the SC-RIS beam is aligned. In addition to picture and data transmissions, another video transmission experiment is conducted for long-term stability tests of the entire system (Supplementary Video 2), where two universal software radio peripheral (USRP) devices are used for higher data transmission rates. The solid experiments on communication systems have demonstrated the autonomous link-enhancing capability of our SC-RIS without BS control.

Conclusions

Our SC-RIS is limited by the dynamic range of the integrated RF detectors. This constrains the system's maximum detection distance. We expect that a 40-dB RF amplifier could increase the detection range from 2 m to 10 m without incurring a notable increase in the system's cost (Supplementary Note 8). The integrated amplifier could also be rerouted to increase the reflective gain of the RIS unit. In addition, the RIS unit could allow a larger portion of the incident power to be detected by the power detector. Currently, the coupler ratio is around –15 dB. However, this approach may induce a larger reflection loss for the RIS unit. We expect that an RF switch or an additional PIN diode could be integrated to control a different power flow in the sensing mode and relay mode, respectively.

The localization algorithm has a computational complexity of $\mathcal{O}(N\log[N])$, where N is the number of RIS units in the system. We note that the current algorithm has a high degree of parallelism and, thus, could be executed more efficiently in a pipeline architecture. In Supplementary Note 9, we demonstrate that the computation cost for a larger-scale SC-RIS system could be optimized to $\mathcal{O}(N_X\log[N_X])$, where N_X is the row or column number of the RIS panel.

We have demonstrated single-user localization by leveraging BS-UE interference on the SC-RIS. In commercial communication systems, dozens of users are usually served by a single BS simultaneously, and thus, dozens of localization problems need to be solved at the same time (multiuser localization). Inspired by the orthogonal frequency-division multiple access³¹ technology that has been widely applied in wireless communication systems, *K* users can directly transmit the EM signals towards the SC-RIS for simultaneous multiuser localization, as long as these users transmit signals that are separate in the frequency domain.

Holographic principles enable applications such as interferometric microscopy³², interference lithography³³ and acoustic holography³⁴. These applications derive their capabilities from three key points. First, the holographic recordings contain complete information of the wavefront, enabling efficient subsequent information processing and intelligent decision-making in complicated environments. In the specific case of information metasurfaces³³⁻³⁶, since microwave signals



Parameter	Value			
Tx power	Approximately -50 dBm to +6 dBm			
Sample rate	20 M samples s ⁻¹			
Bandwidth	8.05 MHz			
Subcarrier spacing	4.88 kHz			
Modulation	16QAM			
Data rate	31.7 Mbps			

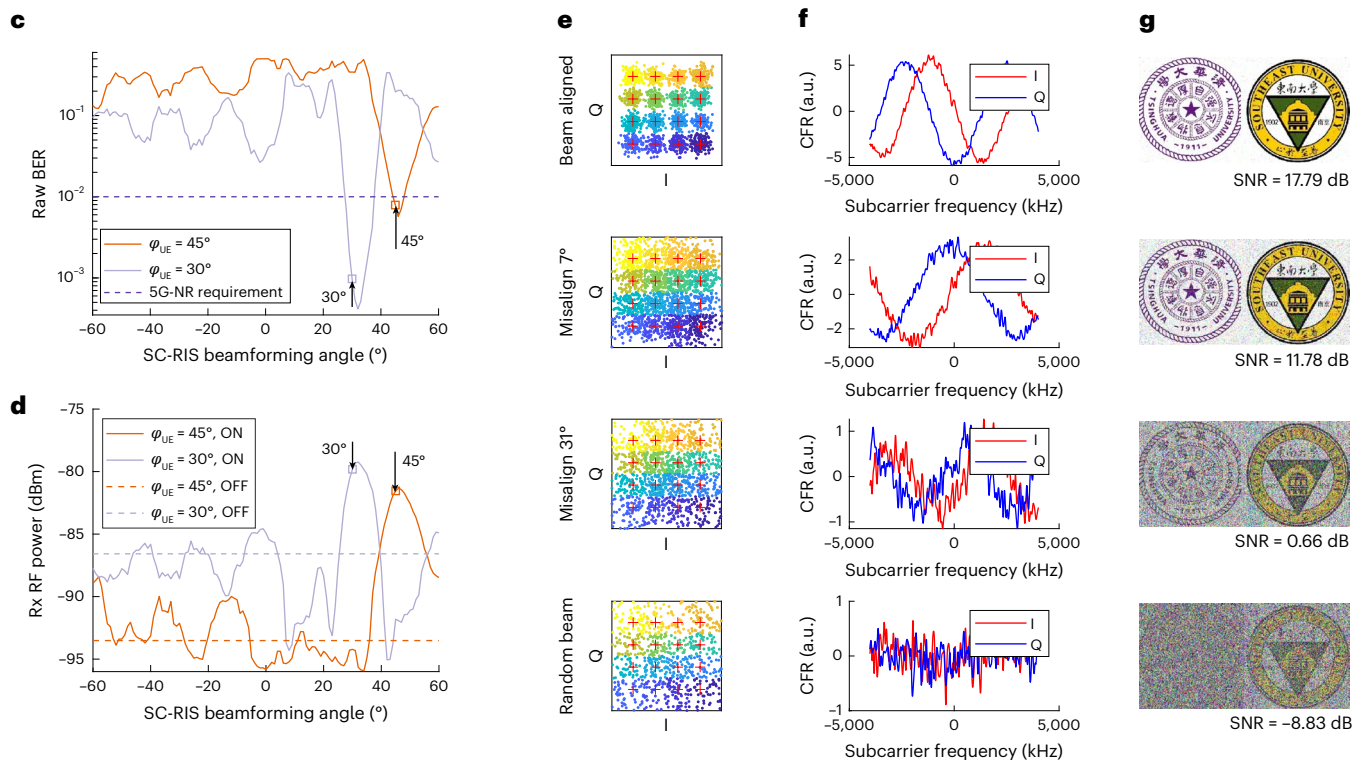


Fig. 6 | **Autonomous beamforming of SC-RIS in a wireless communication system. a**, Photograph of the SC-RIS-aided communication system. Tx, transmitter; Rx, receiver; 5G-NR, fifth-generation new radio. **b**, Key parameters of the implemented OFDM communication system. Tx power means transmit power. **c,d**, BER (**c**) and RF power (**d**) measured by the receiver, presented as a function of the SC-RIS beamforming angles. A substantial BER drop and received RF power rise can be observed when the SC-RIS is ON and correctly

aligns the beam towards the user. **e**, Constellation diagram of the received information-carrying symbols. The symbol noise is reduced when the reflected beam is aligned at the user with autonomous beamforming function activated. **f**, Estimated CFR across the communication bandwidth. I, in-phase component; Q, quadrature component. **g**, Recovered logos of Tsinghua University and Southeast University. The resolution of the reconstructed picture improves when the SC-RIS beam is aligned. SNR, signal-to-noise ratio.

experience fading, random scattering and mutual coupling in complex propagation environments, the wavefront is distorted unpredictably, thereby making the dynamic adaptation of microwave information metasurfaces a key challenge. Our SC-RIS treats these imperfections altogether as a distortion of the wavefront, which is holographically recorded in a physical manner.

Second, non-coherent intensity detectors are usually easy to realize, or in some cases, it is the only choice (such as electron holography). Although non-coherent detectors require a known global reference

wave, this requirement is easily met in the actual SC-RIS-based systems, since coherent microwave illumination is common practice and is typically realized by carrier synchronization. Third, high-performance signal processing is already available in the microwave domain³⁵. In microwave neural networks, microwave signals can be transformed and detected at the speed of light, thereby achieving a higher processing speed of the hologram compared with traditional MCU implementations³⁵. In this way, the SC-RIS may respond much quicker to environmental changes.

Our holographic localization is achieved mainly through the estimation of the user's angular location, with a measured angular resolution of 5.85° using a 32×32 power detector array without the aid of prior channel measurements. Although approaching the theoretical resolution limit, this measured resolution is still not high enough for high-precision wireless applications. This problem could be mitigated by aggregating the measured data in the time domain. Generally, with the number of snapshots being T, the estimator variance will be reduced by a factor of 1/T. Another approach is applying compressive-phase-retrieval-based 36 angular estimators with multipath resolving capability.

Methods

Numerical algorithm

The 2D-FFT is implemented by two consecutive 1D-FFTs, which are applied consecutively to the two indices of the input hologram I_{mn} . The overall 2D-FFT-based holographic localization algorithm is summarized in Algorithm 1. To overcome the signal aliasing caused by the periodicity of the FFT algorithm, we introduce the regulate function in the algorithm to ensure the physical constraint $k_x^2 + k_z^2 \le k_0^2$ on wavenumbers. After the regulation, the location of the user is calculated as

$$\theta_{\rm UE} = -\sin^{-1}\frac{\omega_z}{2\pi}, \quad \varphi_{\rm UE} = \sin^{-1}\left(\frac{\omega_x}{2\pi\cos\theta_{\rm UE}}\right). \tag{3}$$

Algorithm 1. 2D-FFT holographic user localization **Inputs**

The measured hologram $I_{mn} \in \mathbb{R}^{N_z \times N_x} = \mathbb{R}^{32 \times 32}$, power detector spacing $d_z = 2$ cm, $d_x = 2$ cm, operating wavelength $\lambda = 8.57$ cm, BS angular location $(\theta_{BS}, \varphi_{BS})$.

Outputs

Estimated user's location (θ_{UF} , φ_{UF}).

1: $\omega_{x,BS} \leftarrow 2\pi (d_x/\lambda) \cos \theta_{BS} \sin \varphi_{BS}$

2: $\omega_{z.BS} \leftarrow -2\pi (d_z/\lambda) \sin \theta_{BS}$

3: **Compute** 1D-FFT on index m: $\check{I}_{kn} \leftarrow \text{FFT}[I_{mn}], \forall n \in \{0 ... N_x - 1\}$

4: **Compute** 1D-FFT on index n: $\hat{l}_{k\ell} \leftarrow \text{FFT} [\check{l}_{kn}]$

5: **Find** the spectral peak of the hologram: $(i_2, i_k) \leftarrow \arg\max_{(i_2, i_{k'}) \neq (0, 0)} |\hat{I}_{k\ell}|^2$

6: $\Delta_z \leftarrow 2\pi i_z/N_z$, $\Delta_x \leftarrow 2\pi i_x/N_x$

7: $\omega_{z, \text{UF}}^{(1)} \leftarrow \text{regulate} \left(\omega_{z, \text{BS}} + \Delta_z\right)$

8: $\omega_{x.\text{UE}}^{(1)} \leftarrow \text{regulate} \left(\omega_{x,\text{BS}} + \Delta_x\right)$

9: $\omega_{z,\text{UF}}^{(2)} \leftarrow \text{regulate} \left(\omega_{z,\text{BS}} - \Delta_z\right)$

10: $\omega_{x,\text{UE}}^{(2)} \leftarrow \text{regulate} \left(\omega_{x,\text{BS}} - \Delta_x\right)$

11: **Compute** two candidate user's locations $(\theta_{\text{UE}}, \varphi_{\text{UE}})$ by applying equation (3).

Subroutine regulate(x)

R1: **return** $x - 2\pi \cdot \text{round}(x/2\pi)$

SC-RIS hardware platform

In our SC-RIS, each unit is integrated with an RF detector (LMH2110, Texas Instruments), which outputs a voltage proportional to the incident wave power. The 1,024-channel voltages are converted into digital signals using an array of ADC (AD7616, ADI Corporation) and analogue switches (MC74HC4051A, Onsemi). An MCU (STM32F405RGT6, STMicroelectronics) communicates with the ADC array and executes the localization algorithm demonstrated in Algorithm 1 in a sequential way. Once the position of the user is retrieved, the MCU generates the optimized RIS coding based on the 1-bit phase compensation method and transmits the coding patterns to the PIN diode drivers. The above-mentioned procedures cost 6.2 ms altogether (Supplementary Note 11 shows the timing waveforms). The overall system currently draws a maximum power consumption of 60 W. However, we anticipate that the power could be further reduced if the sensing

modules are powered down when the system is not in the sensing mode (Supplementary Note 12).

Communication experiment

In the image transmission experiment, we adopt two SDR devices with RF transceivers (AD9361, Analog Devices) and baseband processors (XC7Z020-CLG484, Xilinx). Both SDR devices are controlled by a personal computer running MATLAB vR2024b, in which the OFDM modulation/demodulation takes place (Supplementary Note 13 shows the detailed OFDM frame format). For the transmitter, the modulation scheme is 16QAM (QAM, quadrature amplitude modulation), with an average transmit power of -50 dBm. A Zadoff-Chu sequence is attached before the OFDM data frames for symbol synchronization. A total number of 1.647 subcarriers are in use, which contain 1.482 data symbols and 165 demodulation reference signals (DMRS, also known as pilot signals). At the receiver, the symbol-level synchronization is first executed based on the Zadoff-Chu sequence, and then carrier frequency offset is estimated and compensated. Finally, DMRS-based channel estimation and data demodulation are executed to recover the image payload.

In the video transmission experiment, to achieve higher data rates, we adopt two USRP devices (USRP-2974, National Instruments) for data transmission tests. The transmitter and receiver USRPs operate at the carrier frequency $f_{\rm c}=3.5\,{\rm GHz}$ with a communication bandwidth of 30 MHz. During video transmission, the physical layer transmitter adopts the standard Long-Term Evolution protocol with modulation and encoding scheme (MCS)-17 (64QAM, $R_{\rm code}\approx0.43$), and the receiver is always configured to the same MCS according to the transmitter. Since the USRP provides a user datagram protocol socket to the application layer, we use Python v3.9 to access these data sockets and transmit the video data payload.

Data availability

The data that support the findings of this study are available from the corresponding authors upon reasonable request.

Code availability

The code that supports the findings of this study are available from the corresponding authors upon reasonable request.

References

- Saad, W., Bennis, M. & Chen, M. A vision of 6G wireless systems: applications, trends, technologies, and open research problems. *IEEE Netw.* 34, 134–142 (2019).
- Khan, L. U., Saad, W., Niyato, D., Han, Z. & Hong, C. S. Digital-twin-enabled 6G: vision, architectural trends, and future directions. *IEEE Comm. Mag.* 60, 74–80 (2022).
- Yang, B. et al. Edge intelligence for autonomous driving in 6G wireless system: design challenges and solutions. *IEEE Wirel.* Comm. 28, 40–47 (2021).
- Wang, Y., Lu, H. & Sun, H. Channel estimation in IRS-enhanced mmWave system with super-resolution network. *IEEE Commun. Lett.* 25, 2599–2603 (2021).
- Li, L. et al. Electromagnetic reprogrammable coding-metasurface holograms. Nat. Commun. 8, 197 (2017).
- Li, W. et al. Intelligent metasurface system for automatic tracking of moving targets and wireless communications based on computer vision. *Nat. Commun.* 14, 989 (2023).
- Li, L. et al. Intelligent metasurfaces: control, communication and computing. eLight 2, 7 (2022).
- 8. Ye, J., Guo, S. & Alouini, M.-S. Joint reflecting and precoding designs for SER minimization in reconfigurable intelligent surfaces assisted MIMO systems. *IEEE Trans. Wirel. Commun.* **19**, 5561–5574 (2020).

- Zhao, H. et al. Metasurface-assisted massive backscatter wireless communication with commodity Wi-Fi signals. *Nat. Commun.* 11, 3926 (2020).
- Pei, X. et al. RIS-aided wireless communications: Prototyping, adaptive beamforming, and indoor/outdoor field trials. *IEEE Trans.* Commun. 69, 8627–8640 (2021).
- Zhang, X. G. et al. An optically driven digital metasurface for programming electromagnetic functions. *Nat. Electron.* 3, 165–171 (2020).
- Aydin, K. et al. Frequency tunable near-infrared metamaterials based on VO₂ phase transition. Opt. Express 17, 18330–18339 (2009).
- Alamzadeh, I., Alexandropoulos, G. C., Shlezinger, N. & Imani, M. F. A reconfigurable intelligent surface with integrated sensing capability. Sci. Rep. 11, 20737 (2021).
- Gu, Z., Ma, Q., Gao, X., You, J. W. & Cui, T. J. Classification of metal handwritten digits based on microwave diffractive deep neural network. Adv. Opt. Mater. 12, 2301938 (2024).
- Zeng, S., Zhang, H., Di, B., Han, Z. & Song, L. Reconfigurable intelligent surface (RIS) assisted wireless coverage extension: RIS orientation and location optimization. *IEEE Comm. Lett.* 25, 269–273 (2021).
- Jian, M. et al. Reconfigurable intelligent surfaces for wireless communications: overview of hardware designs, channel models, and estimation techniques. *Intell. Converg. Netw.* 3, 1–32 (2022).
- 17. You, L. et al. Energy efficiency and spectral efficiency tradeoff in RIS-aided multiuser MIMO uplink transmission. *IEEE Trans. Signal Process.* **69**, 1407–1421 (2021).
- Zhang, X. G. et al. Optoelectronic metasurface for free-space optical-microwave interactions. ACS Appl. Mater. Interfaces 15, 22744–22751 (2023).
- Ma, Q. et al. Smart metasurface with self-adaptively reprogrammable functions. Light: Sci. Appl. 8, 98 (2019).
- Jiang, S., Hindy, A. & Alkhateeb, A. Sensing aided reconfigurable intelligent surfaces for 3GPP 5G transparent operation. *IEEE Trans. Commun.* 71, 6348–6362 (2023).
- Alamzadeh, I. & Imani, M. F. Sensing and reconfigurable reflection of electromagnetic waves from a metasurface with sparse sensing elements. *IEEE Access* 10, 105954–105965 (2022).
- Basar, E. & Poor, H. V. Present and future of reconfigurable intelligent surface-empowered communications. *IEEE Signal Process. Mag.* 38, 146–152 (2021).
- 23. Jiang, R. Z. et al. Simultaneously intelligent sensing and beamforming based on an adaptive information metasurface. *Adv. Sci.* **11**, 2306181 (2024).
- Gong, T. et al. Holographic MIMO communications: theoretical foundations, enabling technologies, and future directions. *IEEE* Commun. Surveys Tuts. 26, 196–257 (2023).
- Ma, Q. et al. Smart sensing metasurface with self-defined functions in dual polarizations. *Nanophotonics* 9, 3271–3278 (2020).
- Benton, S. A. & Bove Jr, V. M. Holographic Imaging (John Wiley & Sons, 2008).
- Zhu, J. et al. Sensing RISs: enabling dimension-independent CSI acquisition for beamforming. *IEEE Trans. Inf. Theory* 69, 3795–3813 (2023).
- 28. Zhang, W. et al. Twin-image-free holography: a compressive sensing approach. *Phys. Rev. Lett.* **121**, 093902 (2018).
- Latychevskaia, T. & Fink, H.-W. Solution to the twin image problem in holography. Phys. Rev. Lett. 98, 233901 (2007).
- 30. Zhou, T. et al. Short-range wireless localization based on meta-aperture assisted compressed sensing. *IEEE Trans. Microw. Theory Techn.* **65**, 2516–2524 (2017).

- Yin, H. & Alamouti, S. OFDMA: a broadband wireless access technology. In Proc. IEEE Sarnoff Symp. 1–4 (IEEE, 2006).
- Ralston, T. S., Marks, D. L., Scott Carney, P. & Boppart, S. A. Interferometric synthetic aperture microscopy. *Nat. Phys.* 3, 129–134 (2007).
- Lu, C. & Lipson, R. H. Interference lithography: a powerful tool for fabricating periodic structures. *Laser Photonics Rev.* 4, 568–580 (2010).
- 34. Hirayama, R. et al. High-speed acoustic holography with arbitrary scattering objects. Sci. Adv. 8, eabn7614 (2022).
- 35. Gao, X. et al. Programmable surface plasmonic neural networks for microwave detection and processing. *Nat. Electron.* **6**, 319–328 (2023).
- Schniter, P. & Rangan, S. Compressive phase retrieval via generalized approximate message passing. *IEEE Trans. Signal Process.* 63, 1043–1055 (2015).

Acknowledgements

L.D. acknowledges financial support from the National Natural Science Foundation of China (grant numbers 62325106 and 62031019) and the National Key Research and Development Program of China (grant number 2023YFB3811503). T.J.C. acknowledges financial support from the National Science Foundation of China (grant number 62288101). We would like to thank Z. Wu, Y. Chen, Y. Cao, Z. Peng and H. Li at Tsinghua University for their voluntary help during the field-test experiments.

Author contributions

J.Z. conceived the idea of holography-inspired SC-RISs, and conducted the theoretical analysis. Z.G. and Q.M. conducted the numerical simulations and fabricated the metasurface. J.Z. and Z.G. conducted the field-test experiments. L.D. and T.J.C. directed and supervised the research. J.Z. and Z.G. processed the data and drafted the original manuscript. All authors discussed the results and commented on the manuscript.

Competing interests

The authors declare no competing interests.

Additional information

Supplementary information The online version contains supplementary material available at https://doi.org/10.1038/s41928-025-01482-3.

Correspondence and requests for materials should be addressed to Jieao Zhu, Ze Gu, Qian Ma, Linglong Dai or Tie Jun Cui.

Peer review information *Nature Electronics* thanks the anonymous reviewers for their contribution to the peer review of this work.

Reprints and permissions information is available at www.nature.com/reprints.

Publisher's note Springer Nature remains neutral with regard to jurisdictional claims in published maps and institutional affiliations.

Springer Nature or its licensor (e.g. a society or other partner) holds exclusive rights to this article under a publishing agreement with the author(s) or other rightsholder(s); author self-archiving of the accepted manuscript version of this article is solely governed by the terms of such publishing agreement and applicable law.

© The Author(s), under exclusive licence to Springer Nature Limited 2025